MATERIALS SCIENCE

Three-dimensional superlattice engineering with block copolymer epitaxy

Jiaxing Ren[1], Tamar Segal-Peretz[2], Chun Zhou[1], Gordon S. W. Craig[1], Paul F. Nealey[1,3]*

Three-dimensional (3D) structures at the nanometer length scale play a crucial role in modern devices, but their fabrication using traditional top-down approaches is complex and expensive. Analogous to atomic lattices, block copolymers (BCPs) spontaneously form a rich variety of 3D nanostructures and have the potential to substantially simplify 3D nanofabrication. Here, we show that the 3D superlattice formed by BCP micelles can be controlled by lithographically defined 2D templates matching a crystallographic plane in the 3D superlattice. Using scanning transmission electron microscopy tomography, we demonstrate precise control over the lattice symmetry and orientation. Excellent ordering and substrate registration can be achieved, propagating through 284-nanometer-thick films. BCP epitaxy also showed exceptional lattice tunability, with a continuous Bain transformation from a body-centered cubic to a face-centered cubic lattice. Lattice stability was mediated by molecular packing frustration, and surface-induced lattice reconstruction was observed, leading to the formation of a unique honeycomb lattice.

INTRODUCTION

One of the central challenges in material science is to predict and control the crystallographic lattice adopted by atoms and molecules. In atomic epitaxy, the lattice parameter and orientation of the epitaxial layer can be manipulated by the underlying substrate (*1*, *2*). The precise control over the lattice geometry of the epitaxial thin film offers the opportunity to create structures with unique electronic, optoelectronic, and magnetic properties (*3*–*5*). Analogous to atomic lattices, block copolymers (BCPs) self-assemble into periodic structures at the nanometer length scale (*6*). In the simplest case of AB diblock copolymers, chemically distinct A and B polymers are covalently bonded together to form a macromolecule that can microphase separate and self-assemble into a variety of morphologies depending on the block chemistries and volume fractions, including lamella, gyroid, cylinder, and sphere. Recent studies using low–molecular weight sphere-forming BCPs demonstrated the formation of quasi-crystalline phases and its dependency on thermal processing history (*7*, *8*). These behaviors are typically observed in metal alloys, suggesting enticing analogies between the fundamental mechanisms governing lattice stability in hard and soft matter.

Building on the concept of atomic epitaxy, the self-assembled structures in BCP thin films can be directed and controlled by substrate templates with topographical features (graphoepitaxy) (*9*–*11*) or chemical contrast (chemoepitaxy) (*12*–*14*). In chemoepitaxy, a thin polymer layer is lithographically defined and chemically modified to form a two-dimensional (2D) guiding template that preferentially interacts with one of the blocks. BCPs are then coated onto the template and self-organize into highly ordered structures in accordance with the lithographic pattern. Directed self-assembly (DSA) of BCPs has mainly focused on perfecting 2D patterns in thin films to be used as an etch mask during semiconductor fabrication (*15*, *16*). However, there is tremendous untapped potential to directly form 3D structures with perfect ordering and substrate registration using BCP epitaxy, greatly simplifying 3D nanofabrication (*17*). Here, we extend the ideas of DSA to explore the design rules for 3D BCP epitaxy. As a model system, we use a sphere-forming BCP, where we consider the minority and majority blocks to form the cores and coronas of micelles, respectively. We use lithographically defined 2D chemical templates to control the symmetries and orientations of the 3D superlattices formed by the BCP micelles. By varying the 2D template designs and the film thicknesses, we examine the lattice stabilities under various strains and the ability of the epitaxy to propagate through thick films. We suggest that the epitaxy of the 3D superlattice formed by BCP micelles provides valuable guidance on the epitaxy of more complex 3D BCP structures such as the gyroid and the lamella-sphere morphology in triblock copolymers. It also offers new insight on the fundamental mechanisms governing symmetry control in soft and hard materials.

RESULTS

Lattice symmetry and orientation control

First, we demonstrated the control over the symmetry and orientation of the BCP superlattice using chemoepitaxy. We used polystyrene-*block*-poly(methyl methacrylate) (PS-*b*-PMMA; 81k-*b*-13k g/mol), which formed micelles with a core of the shorter PMMA block surrounded by a corona of the PS block. In isolation, these micelles are spherical in shape. In the bulk polymer melt, the micelles form space-filling polyhedra and typically adopt a body-centered cubic (BCC) lattice as a result of the competition between the need to uniformly fill space and their tendency to minimize packing frustration (*18*). The period of the bulk BCC lattice was determined by small angle x-ray scattering to be L_{BCC} = 40.1 nm (fig. S1). To guide the assembly of the superlattice, we spin-coated the BCP onto a 2D template (Fig. 1A). The in-plane lattice geometry was controlled by the 2D guiding template, and the out-of-plane lattice parameter was controlled by the BCP film thickness. The template consisted of a PS-wetting background and PMMA-wetting dot arrays that were lithographically defined to match a specific plane in the lattice (fig. S2). The film thickness was carefully controlled to match the corresponding plane spacing. Last, the film was thermally annealed at 190°C for 12 hours. To confirm the 3D structure, we used a back-etch method to prepare the samples on a silicon nitride membrane for scanning transmission electron microscopy (STEM) characterization (*19*).

[1]Pritzker School of Molecular Engineering, University of Chicago, Chicago, IL 60637, USA. [2]Department of Chemical Engineering, Technion–Israel Institute of Technology, Haifa 32000 Israel. [3]Materials Science Division, Argonne National Laboratory, Lemont, IL 60439, USA.
*Corresponding author. Email: nealey@uchicago.edu

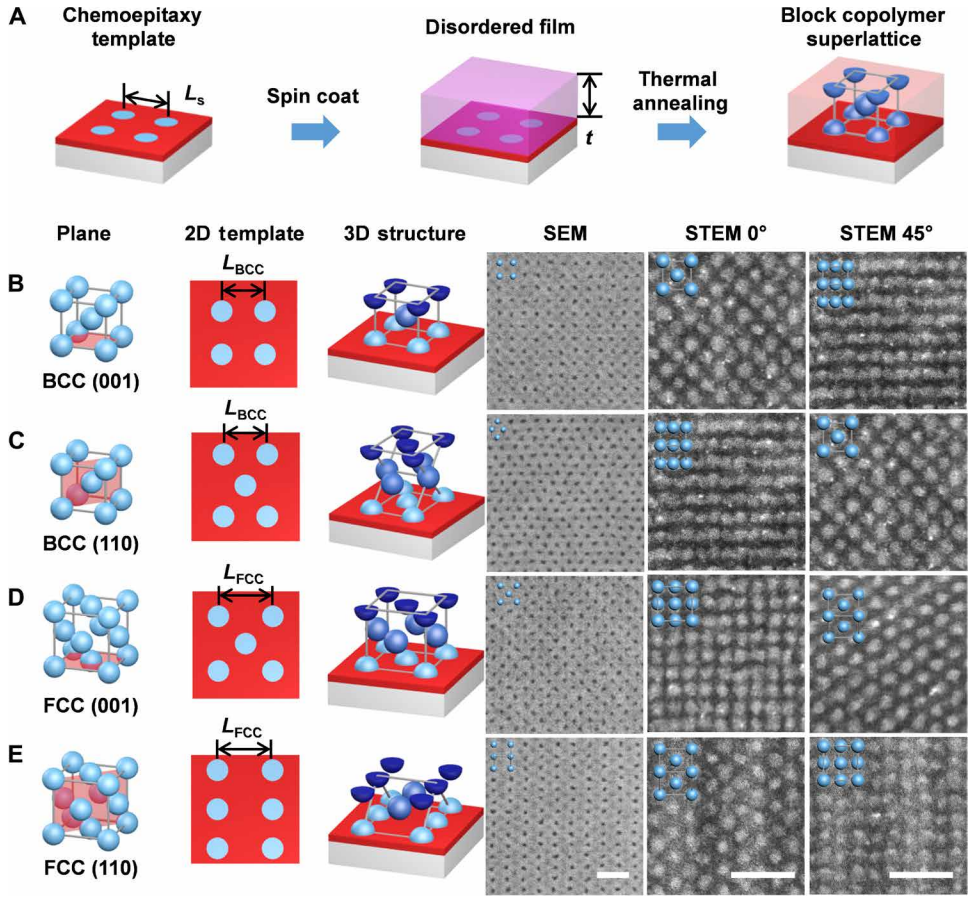

Fig. 1. Controlling the symmetry and orientation of a BCP superlattice. (**A**) Schematic of the chemoepitaxy process flow. A 2D template is lithographically defined. A BCP is then spin coated onto the template. Thermal annealing enables DSA of the BCP into 3D superlattices. (**B** to **E**) Each row refers to the chemoepitaxy of three layers of PS-*b*-PMMA micelles on a specific template pattern: BCC (001), BCC (110), face-centered cubic (FCC) (001), and FCC (110). In each row from left to right, the panels correspond to the following: a unit cell showing the target plane, the 2D layout of the template matching the plane, the 3D structure of the lattice assembled on the template, top-down scanning electron microscopy (SEM) of the assembled sample, and STEM images of the assembled film taken at 0° and 45° sample tilt. For clarity, only the micelle cores are shown in the schematics. In the 3D structure of the assembled film, PMMA cores on different layers were colored in different shades of blue. The insets on the electron microscopy images show the expected structures. Scale bars, 100 nm.

In the case of BCC (001) (Fig. 1B), the template consisted of a square array of dots with pitch $L_S = L_{BCC}$, matching the layout of the BCC (001) plane. The BCP film thickness was also targeted to equal L_{BCC}. After thermal annealing, the scanning electron microscopy (SEM) image of the top surface showed the BCC (001) pattern. 2D STEM images at 0° and 45° sample tilt were in perfect agreement with the projections of the BCC (001) and BCC (110) planes, respectively. To manipulate the lattice type, we first needed to determine the appropriate lattice parameter of the nonbulk lattice. Under the assumption that the volume of the micelles stays constant in different lattice symmetries, the lattice parameter could be calculated by invoking the constraint of the constant volume fraction of the PMMA cores. In the case of face-centered cubic (FCC), the lattice parameter was $L_{FCC} = \sqrt[3]{2}\ L_{BCC} = 50.5$ nm. DSA of FCC (001) could therefore be achieved by matching the 2D template to the FCC (001) plane and the film thickness to L_{FCC} (Fig. 1D). The lattice orientation could be conveniently controlled by matching the 2D template and the film thickness to the layout and spacing of the desired lattice planes. The epitaxy of BCC (110) and FCC (110) are shown in Fig. 1 (C and E), respectively. The ability to stabilize and control the orientations of BCC and FCC lattices is remarkable, as these morphologies are not stable in the thin film with homogeneous boundary conditions. While the BCC is stable in bulk, hexagonal symmetry is preferred by the thin film, as it minimizes the 2D packing frustration. In the absence of the epitaxial template, a previous study has shown that hexagonal monolayers were formed at the substrate surface. As the distance from the substrate increased to >20 layers of micelles, the morphology gradually transitioned into the bulk BCC (*20*).

Three conditions are key for lattice control in the above BCP chemoepitaxy scheme: (i) The 2D template matches the lattice plane; (ii) the film thickness is commensurate with the plane spacing; and (iii) the free surface is nonpreferential. Template matching at BCP microdomain length scales is straightforward in BCP chemoepitaxy, as the template geometry can be arbitrarily defined by lithography; whereas in atomic epitaxy, specific substrate pairings are required. In the vertical direction, the sphere-forming BCP film is spin-coated onto the substrate to a target thickness and is initially in a disordered state. Upon thermal annealing, micelles are formed after microphase separation, and the out-of-plane lattice parameter is determined by the film thickness. This differs from atomic epitaxy, in which the

atoms are deposited sequentially onto the substrate and are not constrained in the direction perpendicular to the substrate. The third condition can be easily fulfilled in the PS-*b*-PMMA system because the two components have similar surface energies at the thermal annealing temperatures (*21*), making the free surface nonpreferential to either block. A previous study has shown that the nonpreferential surface was populated by PMMA hemispheres in a PS matrix and did not have a preference for any particular lattice symmetry, allowing the morphology to be controlled by the substrate (*22*). For BCPs whose blocks have highly different surface energies, the third condition can still be achieved either with solvent vapor annealing (*23*, *24*) or a nonpreferential top coat approach (*25*, *26*), making the chemo-epitaxy scheme generalizable to a wide variety of BCP systems. Because lattice control was based on manipulating boundary conditions, polytypism was observed when different lattice structures shared the same plane layout and plane spacings (fig. S3).

Lattice stability under strain

Lattice strain has a remarkable impact on the physical properties of epitaxial thin films. We studied the BCP superlattice stability under biaxial tensile and compressive strains. On the basis of the epitaxy of BCC (001), we varied the template pitch L_S from 33 to 47 nm and the film thickness from 34.1 to 58.8 nm (fig. S4). The resulting lattices contained three layers of micelles and represented a body-centered tetragonal (BCT) symmetry with in-plane lattice parameter $a = L_S$ and out-of-plane lattice parameter c equals film thickness. This tetragonal distortion connects BCC with FCC and is referred to as the Bain transformation (Fig. 2A) (*27*). We mapped the BCP Bain path with respect to the lattice type, described by c/a, and the normalized unit cell volume V/V_{BCC}, where $V_{BCC} = L_{BCC}^3$ is the unit cell volume of the bulk BCC lattice (Fig. 2B). DSA was characterized with top-down SEM. Three distinctive types of morphologies were observed: (i) well-ordered assembly, (ii) terracing and hole-island formation, and (iii) randomly ordered assembly. Samples are only categorized as "well-ordered" (green) when no terracing was observed in the templated area (100 μm by 100 μm) at low magnification and no random ordering of the micelles was observed at high magnification (fig. S5). Well-ordered pseudomorphic epitaxy (green full circles; Fig. 2B) was achieved for a wide range of c/a ratios, from 0.81 to 1.56, showing a continuous transition along the Bain path from BCC to FCC. The range for V/V_{BCC} was 0.92 to 1.18. Outside of this range, the epitaxy showed poor ordering and terracing (red open circles; Fig. 2B). The blue dotted line in Fig. 2B represents a constant cell volume and is in good agreement with the measured boundaries of the well-ordered assembly over a wide range of c/a.

The change in lattice type and unit cell volume is correlated with the change in shape and volume, respectively, of the individual micelles. The space occupied by each PS-*b*-PMMA micelle can be visualized using Wigner-Seitz cells, as shown by the red polyhedron in Fig. 2C. As all BCT unit cells contain two micelles and the volume fraction of the polymer is constant, the constant unit cell volume indicates that the volume of the micelles was constant. This validates our earlier assumption of constant volume that was used to design the guiding template for nonbulk lattices. The tendency to maintain a constant micelle volume arises from the need to avoid entropic penalties induced by chain stretching or compression. In DSA, the BCP is also subject to the confinements of the film thickness and the guiding template. The additional entropic and enthalpic

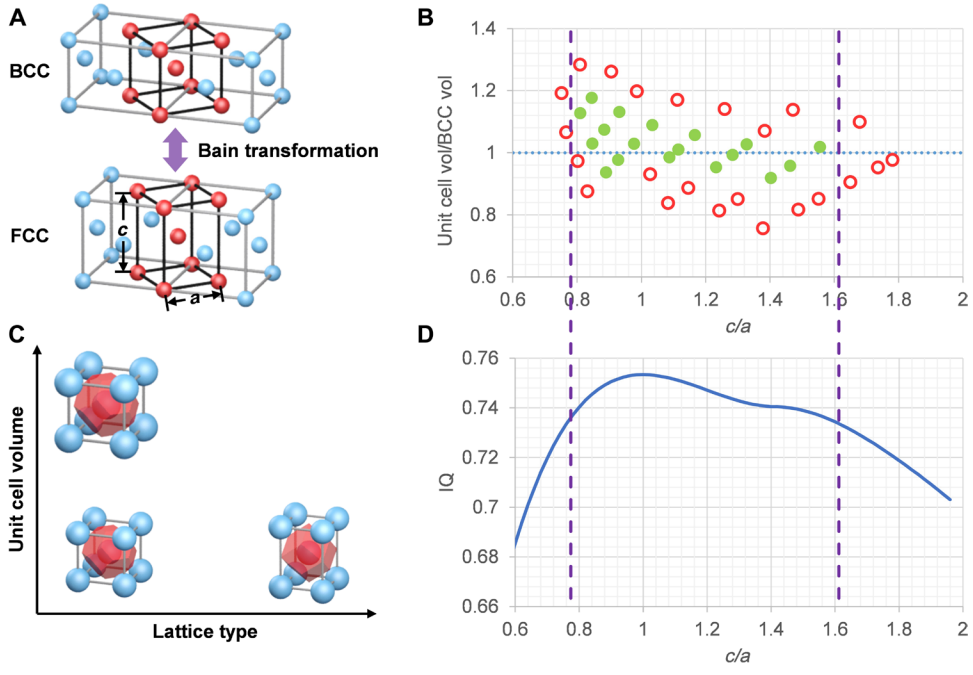

Fig. 2. Bain transformation with 3D DSA. (**A**) BCC and FCC lattices can be connected through Bain transformation. The black lines and red spheres mark the BCT unit cell used to describe this transformation. Sphere diameter is reduced by half for clarity. (**B**) Process window of pseudomorphic epitaxy as shown by normalized unit cell volume versus lattice type. Green full circles represent well-ordered assembly, and red open circles represent films with terracing or random ordering. Blue dotted line signifies the same unit cell volume as that of the bulk BCC. (**C**) Schematics of the BCT unit cells and corresponding Wigner-Seitz cells (red polyhedron) in (B) showing the change in lattice type in the *x* direction and the change in unit cell volume in the *y* direction. (**D**) Sphericity of the Wigner-Seitz cells for different lattice symmetries as measured by the isoperimetric quotient (*IQ*). The purple dashed lines represent the boundary of the process window in (B).

contributions from these thin film boundary conditions help to stabilize deviations from the bulk cell volume by up to 18%. For comparison, atomic epitaxy has no confinement in the direction of film growth, as the atoms are added sequentially and the difference in unit cell volume is typically much smaller, at <5% (*28*).

The shape of the self-assembled micelles results from a balance between the need to uniformly fill the space and the tendency for spherical symmetry. The further a micelle deviates from a spherical shape, the more materials will have to be distorted and redistributed, invoking penalties in free energy. Lee *et al.* (*29*) has shown that the sphericity of the Wigner-Seitz cells can be used to predict the relative stability of BCP lattices. The sphericity can be quantified by the isoperimetric quotient (*IQ*) of the Wigner-Seitz cells, defined as $IQ = 36\pi V^2/S^3$, where V and S are the volume and the surface area of Wigner-Seitz cells, respectively. *IQ* ranges from 0 to 1 with $IQ = 1$ indicating a perfect sphere. We calculated the *IQ* of the Wigner-Seitz cells for different BCT lattices with c/a from 0.6 to 2 (Fig. 2D). The *IQ* reached a maximum of 0.753 when $c/a = 1$, representing the BCC lattice. The maximum *IQ* indicates that BCC requires the least amount of chain stretching, which leads to BCC being the preferred morphology in the bulk. *IQ* dropped monotonically as c/a increased from 1, but there was a shoulder at $c/a = \sqrt{2}$ with $IQ = 0.741$, corresponding to the FCC lattice. Outside of $1 \leq c/a \leq \sqrt{2}$, the sphericity quickly decreased. By mapping the range of c/a where perfect registration was achieved (purple dashed lines; Fig. 2D) onto the *IQ* curve, it can be established that the cutoff *IQ* was 0.740 on the BCC side and 0.737 on the FCC side. Outside of this range, the influence of the template and the film thickness were no longer able to stabilize the distorted tetragonal lattices. The bounds of the epitaxy with respect to the c/a ratios are based on the competition between the need to uniformly fill space and the tendency for spherical symmetry. Therefore, for a sphere-forming BCP, we do not expect the boundaries to change based on polymer chemistry and molecular weight, but we would expect them to shift based on changes in conformational asymmetry or volume fraction of the BCP.

Recent studies by Lee *et al.* (*7*, *29*) and Kim *et al.* (*8*) revealed interesting analogies between the mechanisms of symmetry breaking in BCPs and metal-based systems, showing that the tendency for the BCP to maximize the sphericity of the real-space Wigner-Seitz cells is analogous to the tendency to maximize the Jones zone sphericity in the reciprocal space in the metallic case. For BCPs, the energy difference between different lattice symmetries is relatively low. Self-consistent field theory calculations showed that the difference between BCC and FCC is only 0.5% in terms of their free energy per chain relative to that of the disordered phase (*30*). This allows the template to stabilize the epitaxy film over a wide range of tetragonal distortions from c/a ratios of 0.81 to 1.56. For common rigid metals, straining the lattice by a few percent results in a substantial elastic energy penalty, limiting the strain and film thickness for pseudomorphic epitaxy. However, metal alloys with intrinsic lattice instabilities have much lower energy differences between different crystal structures. For example, full tunability along the Bain path over the c/a range of 1.09 to 1.39 has been demonstrated for Fe-Pd alloys (*31*).

Epitaxy through thick films

We investigated the ability of the template pattern to propagate in the vertical direction. BCP films were assembled with thicknesses from 14.8 to 143.5 nm in ~4-nm intervals on templates matching BCC (001) and FCC (001) patterns. The results show that, for both templates, good registration and ordering were only achieved at quantized film thicknesses (Fig. 3A). When the thickness was not commensurate with the layer spacings for the corresponding template, the assembly either lacked long-range order or formed island-hole structures with well-ordered arrays offset by one layer of micelles (fig. S6). The width of the well-ordered assembly process window stayed relatively constant at less than ±5 nm as the number of layers increased. For the assembly on an FCC (001) template, there was a mismatch between the expected thickness for FCC (green dotted lines; Fig. 3A) and the actual well-ordered assembly process window, which was more obvious in films thicker than 100 nm. By plotting the film thicknesses with perfect assembly against the number of layers and fitting the data with linear regression, we calculated that the layer spacing was 23.9 nm on the FCC (001) template (fig. S7). This represented a 6% difference compared to the expected value of 0.5 L_{FCC} = 25.3 nm. The FCC lattice parameter was calculated under the assumption of constant micelle volume, which was a good approximation but may deviate from the optimal volume. When the commensurability requirement was satisfied, DSA could propagate through 283.9-nm-thick films for both bulk and nonbulk lattices. At 283.9 nm, both BCC (001) and FCC (001) were assembled in the same film with perfect ordering and registration (Fig. 3B), demonstrating the ability of the template to precisely control the position of the micelles hundreds of nanometers from the substrate. This thickness corresponded to 15 and 13 layers of micelles for BCC (001) and FCC (001) patterns, respectively.

The kinetics of BCP epitaxy in films thicker than three times the polymer natural periodicity differ from that in the thin film (*32*). In thin films, the assembly and defect annihilation are cooperative across the film thickness. In thick films, the initial stages of assembly at the

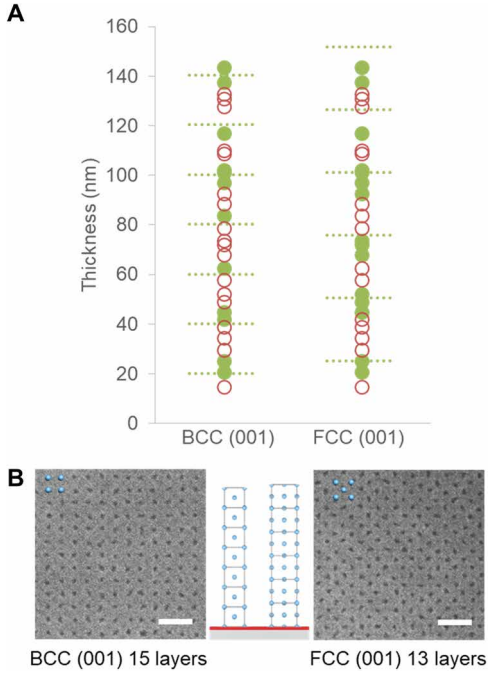

Fig. 3. DSA through thick films. (**A**) DSA on BCC (001) and FCC (001) templates with different film thicknesses. Well-ordered structures (filled green dots) were only achieved when film thickness was commensurate with the corresponding layer spacing (green dotted lines). (**B**) Top-down SEM images of DSA in 283.9-nm-thick film. Scale bars, 100 nm.

free surface occurred independently of the template and lacked any long-range order. After extended annealing, the templated structure eventually dominated and propagated through the entire film thickness, and DSA in films up to 620 nm has been reported (*33*). In films thicker than 1 μm, DSA is limited by the slow dynamics of the BCP. However, in materials with much faster dynamics, the chemical pattern can direct the assembly through much greater thicknesses. For example, epitaxy of 18-μm-thick films has been demonstrated recently with liquid crystals (*34*, *35*).

When the film thickness was incommensurate with the lattice spacing, the Wigner-Seitz cells had to be distorted to fill the space, causing entropic penalties. The film responded by forming either terraces or defects to relieve the distortion (*36*). A similar quantized behavior in assembly was observed in the graphoepitaxy of spheres confined between two trenches with varying widths, where perfect ordering was only achieved with commensurate trench widths (*11*). In atomic epitaxy, the atoms are added sequentially, and the growth modes depend on the interaction strength between the adatoms and the surface. When the adatoms preferentially interact with the surface, the film grows in a layer-by-layer fashion (Frank–van der Merwe growth) (*1*). This is analogous to the one-layer-thick islands formed in BCP epitaxy when the film thickness is incommensurate. The area fraction of the BCP island increases with the film thickness until it forms a complete film at the next commensurate thickness.

Surface-induced lattice reconstruction

In a thin film, the confinements at the substrate interface and free surface break the lattice symmetry, and the energy of DSA becomes dependent on lattice orientation. In the case of BCC (111), the template was a large hexagonal pattern with a center-to-center distance of $\sqrt{2}L_{BCC}$, and the corresponding spacing between each layer was $\sqrt{3}L_{BCC}/6$. The hexagonal pattern matching BCC (111) could be obtained at the top surface only when the DSA film thickness was $\sqrt{3}L_{BCC}/2$, corresponding to three BCC (111) plane spacings and presumably containing four layers of BCP micelles arranged in a hexagonal BCC (111) pattern. STEM tomography (*37*, *38*) revealed that the film consisted of three layers of micelles: A center layer resembling a honeycomb pattern was sandwiched between two layers of hexagonally packed half-micelles at the top and bottom (Fig. 4A). A digitally sliced cross-section (Fig. 4B) shows that the PMMA cores of the micelles on the top and bottom layers sat in the center of the six-member rings of the honeycomb layer. Comparing this unique honeycomb lattice to the BCC lattice with four layers of micelles, the top and bottom layers are the same for both lattices, but the two middle layers of the BCC lattice "merged" into one layer in the honeycomb lattice.

The preference for the honeycomb lattice over the BCC lattice can be understood by analyzing the chain stretching under thin film confinements, visualized by Wigner-Seitz cells (Fig. 4C). If the micelles were to adopt the BCC symmetry, then the surfaces formed by Wigner-Seitz cells would not be flat because of the two middle layers (Fig. 4D). To maintain the BCC lattice and conform to the flat boundary conditions, the PS corona of the two middle layers would need a large amount of redistribution to compensate for the $\sqrt{3}L_{BCC}/12$ protrusions and depressions. Assuming that the length of the polymer chain is ~0.5 L_{BCC}, the distortion corresponds to a ~30% change in chain length, invoking heavy entropic penalties. Instead, the micelles abandoned the BCC symmetry and "shifted" the two middle layers to form one honeycomb layer. For the honeycomb lattice, two species of Wigner-Seitz cells were formed: The honeycomb layer had a volume of 0.987 V_{BCC} and a sphericity of 0.703. The top and bottom layers consisted of half cells, but the corresponding full cells would have a volume of 1.03 V_{BCC} and a sphericity of 0.779. The average sphericity of the system can be estimated by a weighted average of 0.729, close to the sphericity window that we established for the BCT lattices. The topographical confinement from the template limits BCP epitaxy to the lattice symmetries and orientations that can produce a flat surface with its Wigner-Seitz cells to avoid entropic penalties from chain stretching at the surface. We believe that if the corresponding topography could be mimicked on the template surface with advanced patterning methods, then a wider variety of lattice symmetries may be stabilized with BCP epitaxy.

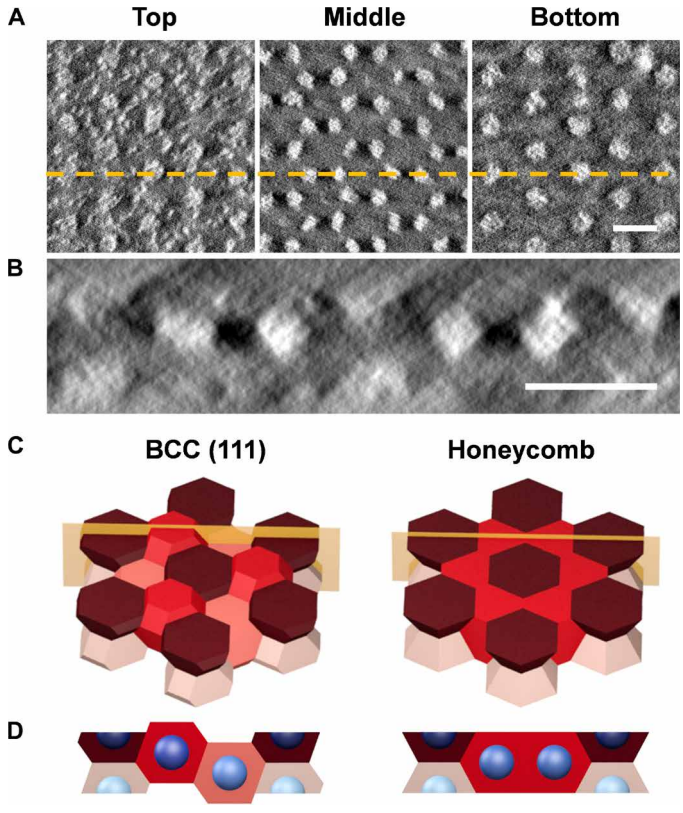

Fig. 4. Formation of honeycomb lattice through lattice distortion. (**A**) In-plane slices created from STEM tomography showing the hexagonal symmetries at the top and bottom layers and the honeycomb symmetry in the middle layer. (**B**) Digitally sliced cross-section along the golden dashed line in (A) showing the three-layer honeycomb lattice. (**C**) 3D schematics of BCC (111) and honeycomb lattice showing the arrangements of the Wigner-Seitz cells. Cells at different layers are colored with different shades of red. (**D**) Cross-section along the golden plane in (C) showing the uneven surfaces of BCC (111) versus the flat surfaces of honeycomb lattice. Scale bars, 50 nm.

DISCUSSION

We have demonstrated a set of design rules for the 3D assembly of BCP micelles using 2D templates. The crystallographic symmetries and orientations can be precisely controlled by template design and film thickness. Single-crystalline domain and perfect registration can be achieved over arbitrarily large areas and through macroscopic thicknesses. The highly ordered and tailorable superlattices have potential applications in photonic and plasmonic material design

(*39*, *40*). Functionalization of the micelles could be achieved by tuning the polymer chemistry (*41*, *42*) or by converting the micelles to metal or metal oxides after assembly (*43*, *44*). These results also demonstrate intriguing analogies between BCP epitaxy and atomic epitaxy. The flexibility afforded by lithographically defined templates offers opportunities to decipher the fundamental principles for symmetry control in condensed matter.

MATERIALS AND METHODS

Materials

Cross-linkable polystyrene (X-PS; AZEMBLY NLD-128) was provided by EMD Performance Materials and used as received. PS-*b*-PMMA [81k-*b*-13k g/mol; M_w/M_n (weight-average molecular weight/number-average molecular weight) = 1.08; product no. P4505-SMMA] was purchased from Polymer Source Inc. and used as received. Silicon wafers coated with 30 nm of silicon nitride on both sides were purchased from WRS Materials. Chemicals and solvents were purchased from Sigma-Aldrich and used as received.

Chemoepitaxy template fabrication and BCP assembly

Chemoepitaxy templates were prepared according to previously reported procedures (*12*, *19*). Briefly, an 8-nm-thick layer of X-PS was spin-coated onto the substrate and thermally cross-linked at 315°C for 5 min in a nitrogen environment. The wafers were then coated with resist and patterned with e-beam lithography (Raith EBPG5200) to form dot patterns with various layouts and pitches. The resist pattern was etched into the X-PS layer using oxygen-containing plasma. After resist removal, PS-*b*-PMMA was spin-coated onto the templates from chlorobenzene solutions with concentrations between 0.5 and 6.0 weight % (wt %) to reach the desired film thickness. To drive DSA of the PS-*b*-PMMA, the samples were annealed in a vacuum chamber at 190°C for 12 hours. Samples thicker than 100 nm were annealed for 72 hours to reach equilibrium.

Membrane fabrication for tomography

Samples for STEM tomography analysis were prepared using a silicon back-etch method as previously reported (*19*). Silicon wafers with silicon nitride coated on both sides were used for sample fabrication. Imaging windows were patterned into the backside nitride, and tungsten alignment marks were deposited onto the front side. Then, chemical patterns were fabricated on the front side using e-beam lithography, and DSA was performed following the procedure described in the above section. After DSA, the wafer was placed in a protective holder that sealed off the front-side polymer film. The setup was then immersed in a 30 wt % potassium hydroxide solution at 90°C. The exposed silicon on the backside was removed until the etching reached the silicon nitride on the front side, creating 30-nm-thick membrane imaging windows. The membrane samples were then treated with sequential infiltration synthesis to stain the PMMA block with alumina (*38*).

Characterization

SEM was performed on a Carl Zeiss Merlin SEM using the in-lens detector at 1 kV voltage. STEM tomography was performed on an FEI Tecnai TEM following a previously reported procedure (*37*). A series of STEM images were acquired at tilt angles ranging from −68° to +68° and reconstructed into a full 3D volume using Inspect 3D software. 2D slices and cross-sections were then extracted from the 3D volume using ImageJ. Film thickness measurements were performed on a JA Woollam alpha-SE ellipsometer at 70° incident angle, and the data were fitted using the Cauchy model.

SUPPLEMENTARY MATERIALS

Supplementary material for this article is available at http://advances.sciencemag.org/cgi/content/full/6/24/eaaz0002/DC1

REFERENCES AND NOTES

1. I. V Markov, *Crystal Growth for Beginners* (World Scientific, 2017).
2. U. W. Pohl, *Epitaxy of Semiconductors* (Graduate Texts in Physics, Springer, 2013).
3. E. C. Nelson, N. L. Dias, K. P. Bassett, S. N. Dunham, V. Verma, M. Miyake, P. Wiltzius, J. A. Rogers, J. J. Coleman, X. Li, P. V. Braun, Epitaxial growth of three-dimensionally architectured optoelectronic devices. *Nat. Mater.* **10**, 676–681 (2011).
4. J. H. Haeni, P. Irvin, W. Chang, R. Uecker, P. Reiche, Y. L. Li, S. Choudhury, W. Tian, M. E. Hawley, B. Craigo, A. K. Tagantsev, X. Q. Pan, S. K. Streiffer, L. Q. Chen, S. W. Kirchoefer, J. Levy, D. G. Schlom, Room-temperature ferroelectricity in strained $SrTiO_3$. *Nature* **430**, 758–761 (2004).
5. A. Winkelmann, M. Przybylski, F. Luo, Y. Shi, J. Barthel, Perpendicular magnetic anisotropy induced by tetragonal distortion of FeCo alloy films grown on Pd(001). *Phys. Rev. Lett.* **96**, 257205 (2006).
6. F. S. Bates, G. H. Fredrickson, Block copolymers—Designer soft materials. *Phys. Today.* **52**, 32 (1999).
7. S. Lee, M. J. Bluemle, F. S. Bates, Discovery of a frank-kasper σ phase in sphere-forming block copolymer melts. *Science* **330**, 349–353 (2010).
8. K. Kim, M. W. Schulze, A. Arora, R. M. Lewis III, M. A. Hillmyer, K. D. Dorfman, F. S. Bates, Thermal processing of diblock copolymer melts mimics metallurgy. *Science* **356**, 520–523 (2017).
9. R. A. Segalman, H. Yokoyama, E. J. Kramer, Graphoepitaxy of spherical domain block copolymer films. *Adv. Mater.* **13**, 1152–1155 (2001).
10. I. Bita, J. K. W. Yang, Y. S. Jung, C. A. Ross, E. L. Thomas, K. K. Berggren, Graphoepitaxy of self-assembled block copolymers on two-dimensional periodic patterned templates. *Science* **321**, 939–943 (2008).
11. J. Y. Cheng, A. M. Mayes, C. A. Ross, Nanostructure engineering by templated self-assembly of block copolymers. *Nat. Mater.* **3**, 823–828 (2004).
12. S. O. Kim, H. H. Solak, M. P. Stoykovich, N. J. Ferrier, J. J. de Pablo, P. F. Nealey, Epitaxial self-assembly of block copolymers on lithographically defined nanopatterned substrates. *Nature* **424**, 411–414 (2003).
13. C.-C. Liu, A. Ramírez-Hernández, E. Han, G. S. W. Craig, Y. Tada, H. Yoshida, H. Kang, S. Ji, P. Gopalan, J. J. de Pablo, P. F. Nealey, Chemical patterns for directed self-assembly of lamellae-forming block copolymers with density multiplication of features. *Macromolecules* **46**, 1415–1424 (2013).
14. S. Ji, L. Wan, C.-C. Liu, P. F. Nealey, Directed self-assembly of block copolymers on chemical patterns: A platform for nanofabrication. *Prog. Polym. Sci.* **54–55**, 76–127 (2016).
15. S. B. Darling, Directing the self-assembly of block copolymers. *Prog. Polym. Sci.* **32**, 1152–1204 (2007).
16. S.-J. Jeong, J. Y. Kim, B. H. Kim, H.-S. Moon, S. O. Kim, Directed self-assembly of block copolymers for next generation nanolithography. *Mater. Today* **16**, 468–476 (2013).
17. C. A. Ross, K. K. Berggren, J. Y. Cheng, Y. S. Jung, J.-B. Chang, Three-dimensional nanofabrication by block copolymer self-assembly. *Adv. Mater.* **26**, 4386–4396 (2014).
18. F. S. Bates, R. E. Cohen, C. V. Berney, Small-angle neutron scattering determination of macrolattice structure in a polystyrene-polybutadiene diblock copolymer. *Macromolecules* **15**, 589–592 (1982).
19. J. Ren, L. E. Ocola, R. Divan, D. A. Czaplewski, T. Segal-Peretz, S. Xiong, R. J. Kline, C. G. Arges, P. F. Nealey, Post-directed-self-assembly membrane fabrication for *in situ* analysis of block copolymer structures. *Nanotechnology* **27**, 435303 (2016).
20. G. E. Stein, E. J. Kramer, X. Li, J. Wang, Layering transitions in thin films of spherical-domain block copolymers. *Macromolecules* **40**, 2453–2460 (2007).
21. P. Mansky, Y. Liu, E. Huang, T. P. Russell, C. Hawker, Controlling polymer-surface interactions with random copolymer brushes. *Science* **275**, 1458–1460 (1997).
22. S. Ji, U. Nagpal, W. Liao, C.-C. Liu, J. J. de Pablo, P. F. Nealey, Three-dimensional directed assembly of block copolymers together with two-dimensional square and rectangular nanolithography. *Adv. Mater.* **23**, 3692–3697 (2011).
23. S. Xiong, L. Wan, Y. Ishida, Y.-A. Chapuis, G. S. W. Craig, R. Ruiz, P. F. Nealey, Directed self-assembly of triblock copolymer on chemical patterns for sub-10-nm nanofabrication *via* solvent annealing. *ACS Nano* **10**, 7855–7865 (2016).
24. X. Gu, I. Gunkel, A. Hexemer, W. Gu, T. P. Russell, An in situ grazing incidence x-ray scattering study of block copolymer thin films during solvent vapor annealing. *Adv. Mater.* **26**, 273–281 (2014).

25. C. M. Bates, T. Seshimo, M. J. Maher, W. J. Durand, J. D. Cushen, L. M. Dean, G. Blachut, C. J. Ellison, C. G. Willson, Polarity-switching top coats enable orientation of sub-10-nm block copolymer domains. *Science* **338**, 775–779 (2012).
26. H. Yoshida, H. S. Suh, A. Ramirez-Hernandez, J. I. Lee, K. Aida, L. Wan, Y. Ishida, Y. Tada, R. Ruiz, J. de Pablo, P. F. Nealey, Topcoat approaches for directed self-assembly of strongly segregating block copolymer thin films. *J. Photopolym. Sci. Technol.* **26**, 55–58 (2013).
27. E. C. Bain, The nature of martensite. *Trans. AIME* **70**, 25 (1924).
28. P. Alippi, P. M. Marcus, M. Scheffler, Strained tetragonal states and bain paths in metals. *Phys. Rev. Lett.* **78**, 3892–3895 (1997).
29. S. Lee, C. Leighton, F. S. Bates, Sphericity and symmetry breaking in the formation of Frank–Kasper phases from one component materials. *Proc. Natl. Acad. Sci. U.S.A.* **111**, 17723–17731 (2014).
30. A. Arora, J. Qin, D. C. Morse, K. T. Delaney, G. H. Fredrickson, F. S. Bates, K. D. Dorfman, Broadly accessible self-consistent field theory for block polymer materials discovery. *Macromolecules* **49**, 4675–4690 (2016).
31. J. Buschbeck, I. Opahle, M. Richter, U. K. Rössler, P. Klaer, M. Kallmayer, H. J. Elmers, G. Jakob, L. Schultz, S. Fähler, Full tunability of strain along the fcc-bcc bain path in epitaxial films and consequences for magnetic properties. *Phys. Rev. Lett.* **103**, 216101 (2009).
32. X. Chen, P. R. Delgadillo, Z. Jiang, G. S. W. Craig, R. Gronheid, P. F. Nealey, Defect annihilation in the directed self-assembly of block copolymers in films with increasing thickness. *Macromolecules* **52**, 7798–7805 (2019).
33. A. M. Welander, G. S. W. Craig, Y. Tada, H. Yoshida, P. F. Nealey, Directed assembly of block copolymers in thin to thick films. *Macromolecules* **46**, 3915–3921 (2013).
34. X. Li, J. J. de Pablo, P. F. Nealey, J. A. Martinez-Gonzalez, in *Emerging Liquid Crystal Technologies XIII*, I. Muševič, L.-C. Chien, D. J. Broer, V. G. Chigrinov, Eds. (SPIE, 2018), vol. 10555, pp. 1–40.
35. J. A. Martínez-González, X. Li, M. Sadati, Y. Zhou, R. Zhang, P. F. Nealey, J. J. de Pablo, Directed self-assembly of liquid crystalline blue-phases into ideal single-crystals. *Nat. Commun.* **8**, 15854 (2017).
36. H. Yokoyama, T. E. Mates, E. J. Kramer, Structure of asymmetric diblock copolymers in thin films. *Macromolecules* **33**, 1888–1898 (2000).
37. T. Segal-Peretz, J. Ren, S. Xiong, G. Khaira, A. Bowen, L. E. Ocola, R. Divan, M. Doxastakis, N. J. Ferrier, J. de Pablo, P. F. Nealey, Quantitative three-dimensional characterization of block copolymer directed self-assembly on combined chemical and topographical prepatterned templates. *ACS Nano* **11**, 1307–1319 (2017).
38. T. Segal-Peretz, J. Winterstein, M. Doxastakis, A. Ramírez-Hernández, M. Biswas, J. Ren, H. S. Suh, S. B. Darling, J. A. Liddle, J. W. Elam, J. J. de Pablo, N. J. Zaluzec, P. F. Nealey, Characterizing the three-dimensional structure of block copolymers *via* sequential infiltration synthesis and scanning transmission electron tomography. *ACS Nano* **9**, 5333–5347 (2015).
39. M. R. Jones, K. D. Osberg, R. J. MacFarlane, M. R. Langille, C. A. Mirkin, Templated techniques for the synthesis and assembly of plasmonic nanostructures. *Chem. Rev.* **111**, 3736–3827 (2011).
40. J. A. Fan, C. Wu, K. Bao, J. Bao, R. Bardhan, N. J. Halas, V. N. Manoharan, P. Nordlander, G. Shvets, F. Capasso, Self-assembled plasmonic nanoparticle clusters. *Science* **328**, 1135–1138 (2010).
41. V. P. Chuang, J. Y. Cheng, T. A. Savas, C. A. Ross, Three-dimensional self-assembly of spherical block copolymer domains into V-shaped grooves. *Nano Lett.* **6**, 2332–2337 (2006).
42. G. R. Whittell, M. D. Hager, U. S. Schubert, I. Manners, Functional soft materials from metallopolymers and metallosupramolecular polymers. *Nat. Mater.* **10**, 176–188 (2011).
43. Q. Peng, Y.-C. Tseng, S. B. Darling, J. W. Elam, A route to nanoscopic materials *via* sequential infiltration synthesis on block copolymer templates. *ACS Nano* **5**, 4600–4606 (2011).
44. J. Chai, D. Wang, X. N. Fan, J. M. Buriak, Assembly of aligned linear metallic patterns on silicon. *Nat. Nanotechnol.* **2**, 500–506 (2007).

Acknowledgments

Funding: We acknowledge support by the U.S. Department of Energy (DOE), Office of Science, Basic Energy Sciences, Materials Sciences and Engineering Division. This research used resources of the Center for Nanoscale Materials, a DOE Office of Science User Facility operated for the DOE Office of Science by Argonne National Laboratory under contract no. DE-AC02-06CH11357. We acknowledge the University of Chicago Research Computing Center for support of this work. We acknowledge the MRSEC Shared User Facilities at the University of Chicago (NSF DMR-1420709). This research used resources of the Advanced Light Source, which is a DOE Office of Science User Facility under contract no. DE-AC02-05CH11231. T.S.-P. is an Azriely Fellow, supported by the Azriely Foundation. **Author contributions:** P.F.N. designed and directed the study. J.R. performed sample fabrication, characterization, and data analysis. T.S.-P. and C.Z. performed the tomography experiments. J.R., G.S.W.C., and P.F.N. wrote the manuscript with contributions from all the authors. **Competing interests:** The authors declare that they have no competing interests. **Data and materials availability:** All data needed to evaluate the conclusions in the paper are present in the paper and/or the Supplementary Materials. Additional data related to this paper may be requested from the authors.

Submitted 10 August 2019
Accepted 1 May 2020
Published 12 June 2020
10.1126/sciadv.aaz0002

Citation: J. Ren, T. Segal-Peretz, C. Zhou, G. S. W. Craig, P. F. Nealey, Three-dimensional superlattice engineering with block copolymer epitaxy. *Sci. Adv.* **6**, eaaz0002 (2020).